

# The distant young embedded stellar cluster CBJC 8 associated with G085.40-0.00<sup>★,★★</sup>

P. Persi<sup>1</sup>, M. Tapia<sup>2</sup>, and M. Gómez<sup>3</sup>

<sup>1</sup> INAF-IASF, Sez. di Roma, via Fosso del Cavaliere 100, 00133 Roma, Italy  
e-mail: paolo.persi@iasf-roma.inaf.it

<sup>2</sup> Instituto de Astronomía, Universidad Nacional Autónoma de México, Apartado Postal 877, Ensenada, Baja California, CP 22830, Mexico  
e-mail: mt@astrosen.unam.mx

<sup>3</sup> Observatorio Astronómico de Córdoba, Córdoba, Argentina  
e-mail: mercedes@oac.uncor.edu

Received 12 April 2010 / Accepted 30 September 2010

## ABSTRACT

**Context.** The infrared cluster CBJC 8 is associated with a 6.7 GHz methanol maser and a compact radio-continuum source, G85.40-0.00. It is located at a distance of about 8 kpc.

**Aims.** The aim is to study the characteristics of this distant and compact embedded cluster and derive the properties of its stellar population.

**Methods.** We present new ground-based near- and mid-infrared imaging observations of this region. The calibrated images were analysed together with archive *Spitzer* IRAC images.

**Results.** Based on the discovery of a considerable fraction of embedded sources with infrared excess emission that are concentrated within a radius around 16'' centred near the position of the compact HII region G85.40-0.00, we were able to confirm the presence of a very young embedded cluster. It was found to contain more than 58 members brighter than  $M_K = 2.6$ , two-thirds of which showing significant near- or mid-IR excess emission. We present spectral energy distributions and extrapolated total luminosities for nine sources with large mid-infrared excesses that were measured in all four IRAC bands. For the brightest of these, G8540A, which is associated with a methanol maser and a compact HII region, we fitted a model of an infalling envelope plus disc plus central star to its observed 1.6 to 850  $\mu\text{m}$  fluxes to get an idea of its physical properties. We also report a single 2.12  $\mu\text{m}$  molecular hydrogen line emission knot near the centre of the cluster, which support the idea about an outflow activity.

**Key words.** stars: formation – HII regions – ISM: clouds – masers – stars: protostars – ISM: jets and outflows

## 1. Introduction

It is widely accepted that most, if not all, intermediate- to high-mass stars are born in clusters (e.g. Lada & Lada 2003). When very young, they are still embedded in dense molecular cores as products of the fragmentation of a large parental cloud (e.g. Bonnell & Bates 2006). Consequently, these young clusters are highly extinguished and are undetectable at visible wavelengths. Infrared imaging and spectroscopy are required to identify and investigate their properties, which then leads to a better understanding of the physical conditions of their environment and of their young stellar members (Lada & Lada 2003, and references therein). Embedded clusters are therefore extremely important

targets for investigating the early stages of star formation and stellar evolution.

Naturally, most of the available infrared surveys of high-mass star-forming regions are focused on relatively nearby regions, chosen because of the presence of HII regions (via radio-continuum or line emission), warm and dense molecular clouds (via emission in CO or other molecules) or masers (e.g. water and methanol) characteristic of massive star-formation. A large number of embedded clusters have also been discovered by searching for concentrations of near-IR sources in large-scale infrared surveys, like 2MASS (Skrutskie et al. 2006). Using this data-base, Dutra et al. (2003) and Bica et al. (2003b) have discovered several hundred possible young clusters, many of them seen at optical wavelengths. In addition to a compilation from the literature by Bica et al. (2003a), there are now more than 660 catalogued infrared clusters, stellar groups, and candidates. These authors, considered that more than 60% of their sample is located at heliocentric distances of  $d < 3$  kpc and only some 10% at distances larger than 7 kpc. Because of their faintness, only a small number of the latter have been studied in detail (e.g. Bohigas & Tapia 2003). The characterization of the properties of as many clusters as possible, especially in different environments, should serve to better understand the large-scale mechanisms that lead to high-mass cluster formation.

\* Based on observations made with the Italian Telescopio Nazionale Galileo (TNG), operated on the island of La Palma by the Fundacion Galileo Galilei of the INAF (Istituto Nazionale di Astrofisica) at the Spanish Observatorio del Roque de los Muchachos of the Instituto de Astrofísica de Canarias, and at the Observatorio Astronómico Nacional, San Pedro Mártir, B.C, Mexico. This work uses archive observations made with the *Spitzer Space Telescope*, which is operated by the Jet Propulsion Laboratory, California Institute of Technology under a contract with NASA.

\*\* The photometric data tables are only available in electronic form at CDS via anonymous ftp to [cdsarc.u-strasbg.fr](mailto:cdsarc.u-strasbg.fr) (130.79.128.5) or via <http://cdsweb.u-strasbg.fr/viz-bin/qcat?J/A+A/525/A1>



**Fig. 1.**  $111'' \times 111''$  colour-coded image of the region centred at (J2000)  $\alpha = 20^{\text{h}}54^{\text{m}}14.3^{\text{s}}$ ,  $\delta = 44^{\circ}54'05''$ , made from the  $J$  (blue),  $H$  (green), and  $K$  (red) individual images. The yellow circle of radius  $15.5''$  marks the formal boundaries of the young cluster CBJC 8, centred at  $\alpha = 20^{\text{h}}54^{\text{m}}14.21^{\text{s}}$ ,  $\delta = 44^{\circ}54'07.4''$  (see Sect. 3). North is at the top and east to the left.

CBJC 8 is a very compact, embedded cluster discovered by Cambr esy et al. (2002) while studying the interstellar extinction distribution in a large area of the North American and Pelican nebulae (NAPN) complex by using 2MASS photometry. A by-product of their extinction-mapping method, based on comparing  $K$ -band star counts and  $(H - K)$  colour-index distributions, was to locate even quite faint embedded clusters in a very efficient way. Among these, CBJC 8 stands out for containing a 6.7 GHz methanol maser close to its centre, found and catalogued as G85.40-0.00 by Pestalozzi et al. (2005) and an associated radio HII region, G085.4102+00.0032 (Urquhart et al. 2009). The cluster lies in a region of the northern NAPN complex, away from the line of sight of highest obscuration. Based on some properties of the cluster, such as a small angular size and faintness, which widely differ from the embedded clusters associated with the NAPN complex (at  $d \approx 600$  pc), Cambr esy et al. (2002) argued that CBJC 8 should be located at a much farther distance, in the Perseus arm. This young complex is also identified as RMS 3878 in the red MSX source (RMS) survey (Urquhart et al. 2008b). Radial velocities from the CO and  $\text{NH}_3$  line emission ( $V_{\text{LSR}} = -36.5 \text{ km s}^{-1}$ , Urquhart et al. 2008a;  $V_{\text{LSR}} = -35.4 \text{ km s}^{-1}$ , Urquhart et al. 2010<sup>1</sup>), and from the maser lines ( $V_{\text{LSR}} = -29.5$  to  $-33.0 \text{ km s}^{-1}$ , Pestalozzi et al. 2005) imply, using Brand & Blitz’s (1993) rotation curve, kinematical distances in the range 6.8–10 kpc. Throughout this work, a distance from the Sun to CBJC 8 of 8.0 kpc will be assumed.

In order to derive the characteristics of this embedded stellar cluster located in the outer Galaxy, and to study the nature of its stellar population, we obtained flux-calibrated high-resolution

near- and mid-infrared images of the area containing CBJC 8. These were supplemented with archive *Spitzer* IRAC data that will be described in Sect. 2. We discuss in Sect. 3 the distribution and the colour–colour and colour–magnitude plots that resulted from the photometry; the spectral energy distributions (SEDs) for the most luminous mid-infrared sources believed to form the core of this cluster were constructed and analysed. Finally, our conclusions are listed in Sect. 4.

## 2. Observations

### 2.1. Near-infrared images

Near-infrared images through narrow-band  $H_2$  ( $\lambda_0 = 2.122 \mu\text{m}$ ,  $\Delta\lambda = 0.032 \mu\text{m}$ ) and  $K_{\text{cont}}$  ( $\lambda_0 = 2.270 \mu\text{m}$ ,  $\Delta\lambda = 0.034 \mu\text{m}$ ) filters, as well as through standard broad-band  $JHK$  filters, were collected on the nights of 2008 July 12 and 14 using the Near Infrared Camera Spectrometer (NICS) attached to the 3.58 m Telescopio Nazionale Galileo (TNG) at the Observatorio del Roque de los Muchachos on La Palma island. The NICS has a HgCdTe Hawaii 1024  $\times$  1024 array and was used in the SF (small field) configuration that provides a scale of  $0.13''/\text{pixel}$ . In each band, 9 dithered frames spaced by  $10''$  were taken and coadded, for total on-source integration times of 630 s, 540 s and 360 s for  $J$ ,  $H$ , and  $K$ , respectively. The total integration time for each of the narrow-band ( $H_2$  and  $K_{\text{cont}}$ ) filters was 1170 s. All images were centred at (J2000)  $\alpha = 20^{\text{h}}54^{\text{m}}14.3^{\text{s}}$ ,  $\delta = 44^{\circ}54'05''$  and covered an area of  $111'' \times 111''$ . The images were reduced with SNAP, a pipeline for infrared imaging data at TNG. Figure 1 shows a colour-coded image obtained by combining the  $J$  (blue),  $H$  (green) and  $K$  (red) individual images of the region G85.40-0.00. In this figure, the presence of a cluster of very red

<sup>1</sup> Data available in the RMS Database Server [http://www.ast.leeds.ac.uk/cgi-bin/RMS/RMS\\_DATABASE.cgi](http://www.ast.leeds.ac.uk/cgi-bin/RMS/RMS_DATABASE.cgi)

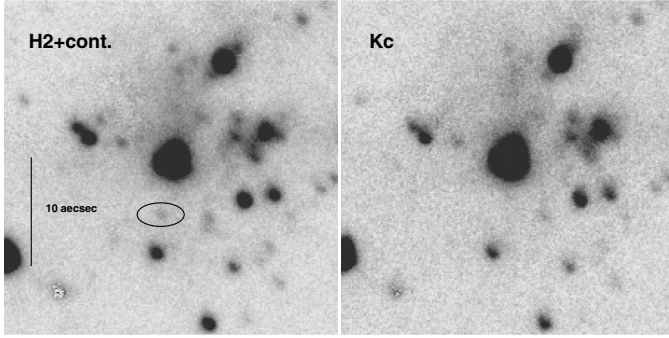


**Fig. 2.**  $H_2$  ( $2.12 \mu\text{m}$ ) and  $K_{\text{cont}}$  ( $2.27 \mu\text{m}$ ) images of the  $30'' \times 30''$  field centred on G85.40+0.00 as in Fig. 1. The ellipse indicates the position of the  $H_2$  emission knot.

objects close to the centre is evident. It is surrounded by a faint, roundish, diffuse nebula of  $\sim 15''$  in size. That it is seen in all bands suggests a reflection origin. We note the discovery of a faint,  $H_2$  emission knot at the position  $\alpha = 20^{\text{h}}54^{\text{m}}14.45^{\text{s}}$   $\delta = 44^{\circ}54'00.0''$  (J2000), near the centre of the embedded cluster. This is marked in Fig. 2, which shows narrow-band images of the central region in the molecular hydrogen line at  $2.12 \mu\text{m}$  compared with its neighbouring continuum at  $2.27 \mu\text{m}$ .

All images were calibrated with the photometric standard stars from Hunt et al. (1998) and Persson et al. (1998). The measured  $FWHM$  of the point-spread function (PSF) is between  $0.6''$  and  $0.8''$ .  $JHK$  photometry was obtained using DAOPHOT (Stetson 1987) within IRAF<sup>2</sup> in the standard way, with an aperture of  $1''$ . For the crowded regions, we used the PSF-fitting procedure included in DAOPHOT. The limiting magnitudes were around 20.5, 19.5 and 18.3 mag in  $J$ ,  $H$  and  $K$ , respectively. In the  $K$  band, we detected 402 sources in an area of  $111'' \times 111''$ . The table listing all the individual  $JHK$  photometric measurements is only available electronically through SIMBAD<sup>3</sup>.

## 2.2. Spitzer IRAC images

The archive IRAC images at  $3.6$ ,  $4.5$ ,  $5.8$  and  $8.0 \mu\text{m}$  of G85.40-0.00 studied here are part of the *Spitzer* Space Telescope project entitled “IRAC and MIPS observations of the North American and Pelican Nebula” (L. Rebull, PI). It consists of an imaging study of more than 4 square degrees of the sky. The observations and statistical results of this large-scale study are described by Guieu et al. (2009). We have analysed only a very small portion of these images centred at the position of G85.40-0.00. Figure 3 displays the  $4.5 \mu\text{m}$  image of a  $3' \times 3'$  field. The  $3.6$  and  $4.5 \mu\text{m}$  images exhibit mostly stellar radiation, while the  $5.8$  and  $8 \mu\text{m}$  bands are dominated by cooler dust and PAH emission.

Thirty-two point-like sources were detected and measured at  $3.6 \mu\text{m}$  in our  $JHK$  field, of which only twelve were measurable in all four IRAC bands. We performed photometry of these sources using the DAOPHOT package within IRAF with an aperture of 3 pixels ( $\sim 3.7''$ ) and a sky annulus extending from 3 to 7 pixels. In the crowded regions, the sky was chosen appropriately for each object to avoid contamination. We applied the corresponding aperture corrections and the zero magnitude

<sup>2</sup> IRAF is distributed by the National Optical Astronomy Observatories, which are operated by the Association of Universities for Research in Astronomy, Inc., under cooperative agreement with the National Science Foundation.

<sup>3</sup> <http://cdsweb.u-strasbg.fr/viz-bin/qcat?J/A+A/525/A1>

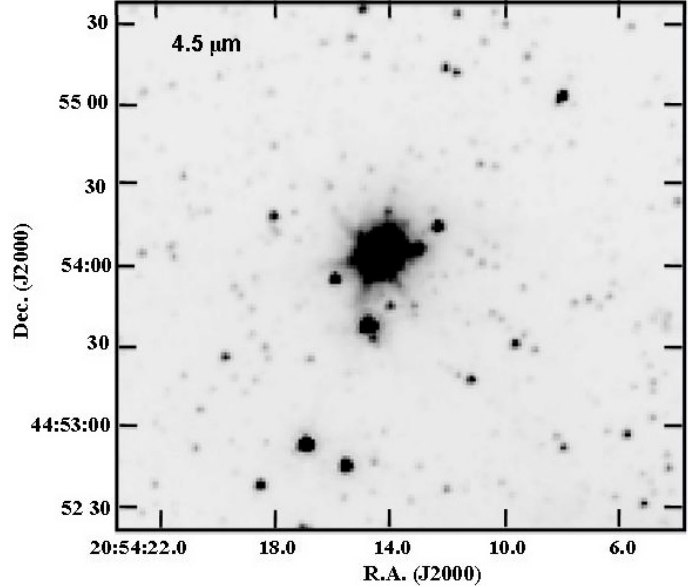


**Fig. 3.** IRAC  $4.5 \mu\text{m}$  image of G85.40-0.00 centred as in Fig. 1.

fluxes from the *Spitzer* IRAC user manual v.5.0. In the central  $60'' \times 60''$ , nine sources were detected and measured in the four bands. The photometry from the IRAC frames is listed in a table only available electronically through SIMBAD<sup>4</sup>.

The brightest and reddest objects in our sample are identified on the multiwavelength mosaic of the central  $20'' \times 13''$  field presented in Fig. 4. The archive  $70 \mu\text{m}$  MIPS image is dominated by a single bright source centred at  $\alpha = 20^{\text{h}}54^{\text{m}}13.7^{\text{s}}$   $\delta = 44^{\circ}54'07.3''$  (J2000). We measured it photometrically using an aperture of 3.6 pixels and a sky annulus extending from 4.0 to 6.6 pixels, and the corresponding aperture correction from the MIPS Data Handbook v.3.2.1 was applied. The measured flux density was  $337.6 \text{ Jy}$ . The peak emission at  $70 \mu\text{m}$  lies within a few arcseconds of the measured position of the mid-infrared source A and coincides with the  $450$  and  $840 \mu\text{m}$  peak emission reported by Di Francesco et al. (2008)

## 2.3. Ground-based mid-infrared images

Mid-infrared images at  $8.9$ ,  $9.9$ ,  $12.7$ , and  $18.7 \mu\text{m}$  of G85.40-0.00 were taken on the night of 2006 November 7 with the mid-infrared camera CID (Salas et al. 2006) on the 2.1 m telescope of the Observatorio Astronómico Nacional at San Pedro Mártir, Baja California, Mexico. This camera is equipped with a Rockwell  $128 \times 128$  pixel Si:As BIB detector array that delivers an effective scale of  $0.55''/\text{pix}$ . The images were taken in the standard chop-nodding mode to remove the sky and telescope emission background. The standard stars  $\alpha$  Lyr,  $\beta$  Peg,  $\beta$  And,  $\gamma$  Aql, and  $\mu$  Cep were observed before and after the programme source at similar air-masses for flux calibration and to measure the point-spread function (PSF) at each wavelength. These values ranged from  $\sim 1.6$ – $1.8''$  ( $FWHM$ ) at the shorter wavelengths, to  $\sim 2.6''$  at  $18.7 \mu\text{m}$ .

Figure 4 illustrates multiwavelength images from  $2.2$  to  $18.7 \mu\text{m}$  of the central region of G85.40-0-00, including our new ground-based near- and mid-infrared frames as well as the *Spitzer* IRAC observations. The two brightest mid-infrared sources A and B were measured photometrically on the CID

<sup>4</sup> <http://cdsweb.u-strasbg.fr/viz-bin/qcat?J/A+A/525/A1>

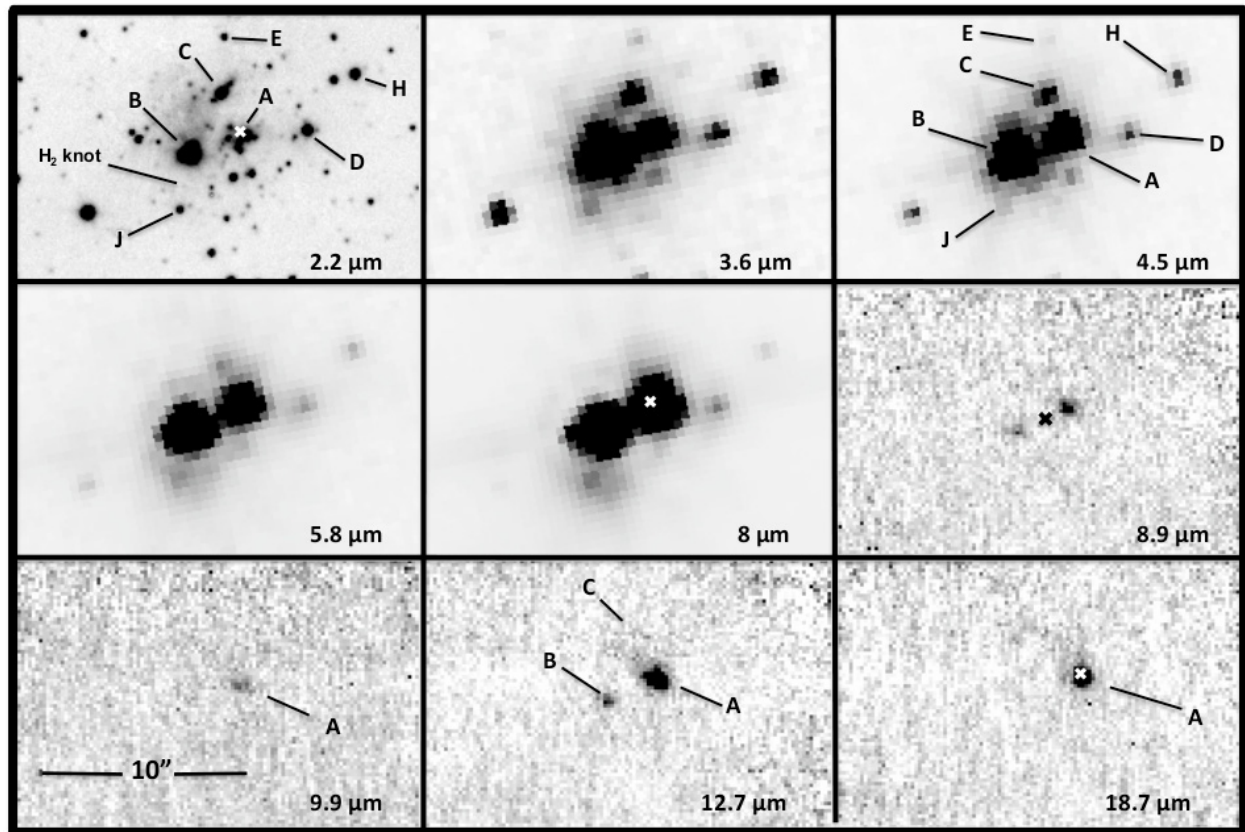


**Fig. 4.** Multiwavelength 2 to 19  $\mu\text{m}$  mosaic of a  $20'' \times 13''$  region centred on G85.40+0.00. Each panel shows at the same scale the emission structure at the corresponding wavelength. The mid-infrared sources with excess emission are labeled A to J. The white crosses on each of the 2.2, 8, and 18.7  $\mu\text{m}$  panels mark the position of the 6.7 GHz methanol maser (Pestalozzi et al. 2005), which coincides with that of the compact radio HII region (Urquhart et al. 2009), the emission peaks of the *MSX* source at 21.3  $\mu\text{m}$ , and the MIPS (70  $\mu\text{m}$ ) and SCUBA (450 and 850  $\mu\text{m}$ , Di Francesco et al. 2008) sources. The black cross on the 8.9  $\mu\text{m}$  panel marks the centroid of the 8.28  $\mu\text{m}$  *MSX* source.

**Table 1.** Mid-infrared magnitudes and errors of sources G8540 A and G8540 B as measured on our CID images.

Source	[8.9] mag	[9.9] mag	[12.7] mag	[18.7] mag
G85.40 A	4.33 (0.16)	4.13 (0.27)	1.54 (0.05)	-0.55 (0.05)
G85.40 B	5.29 (0.39)	–	3.54 (0.22)	–

calibrated images with a  $4''$  aperture and their mid-infrared magnitudes and statistical errors are given in Table 1. The brightest of these, labeled A, coincides with the 6.7 GHz methanol maser listed in the catalogue by Pestalozzi et al. (2005), and with the peak emission of the MIPS (70  $\mu\text{m}$ ) and SCUBA (450 and 850  $\mu\text{m}$ , Di Francesco et al. 2008) sources. In the *MSX* survey images, sources A and B are unresolved ( $FWHM \sim 21''$ ), but we noted that the centroid of the *MSX* source shifted monotonically with wavelength. In channel E (21.3  $\mu\text{m}$ ), the centroid coincides with the position of G8540 A, but in channel A (8.28  $\mu\text{m}$ ), the centroid corresponds to a point between G8540 A and G8540 B, which is totally consistent with the individual mid-infrared colour of each of these sources, as clearly seen in the higher resolution CID images (see Fig. 4).

### 3. Discussion

#### 3.1. Source counts and infrared colour–colour diagrams

Using 2MASS data Cambr esy et al. (2002) first reported the presence of a small number of enhanced source-density regions

associated with higher than expected extinction in the periphery of the North America and Pelican nebulae. The authors identified them as embedded cluster candidates and described their cluster No. 8 as “very compact, which might indicate a large distance ... containing 12 stars”, though only six of these had at least one colour index ( $H - K$ ) measured by 2MASS. It was the discovery of a methanol maser source at the centre of CBIC-8 by Pestalozzi et al. (2005) that provided firm evidence of its young age and high mass. This was further strengthened by associations with a compact HII region and CO and ammonia clouds that were discovered later (Urquhart et al. 2008a, 2009). The range of kinematic distances to these line-emitting sources led us to adopt a heliocentric distance of 8 kpc to this young complex, placing it in the Perseus arm.

By means of  $K$ -band source counts in concentric rings down to our sensitivity limit ( $K \leq 19$ ), we confirmed the reality of the embedded cluster and determined its precise centre and extension, assuming spherical geometry. The radial plot of the projected source density is presented in Fig. 5. The radius at which the source density reaches that of the surrounding field was found to be  $15.5''$ , which we consider to be the formal radius of the cluster although, as will be discussed below, a few bright members lie outside these boundaries. We measured the coordinates of the centre of CBIC-8 to be  $\alpha = 20^{\text{h}}54^{\text{m}}14.21^{\text{s}}$ ,  $\delta = 44^{\circ}54'07.4''$  (J2000). The circle delimiting the “cluster area” is drawn in Fig. 1.

Figure 6 shows the  $J - H$  versus  $H - K$  and  $H - K$  versus  $K - [3.6]$  diagrams of all sources measured in these colours. Filled circles represent sources located within the cluster limits

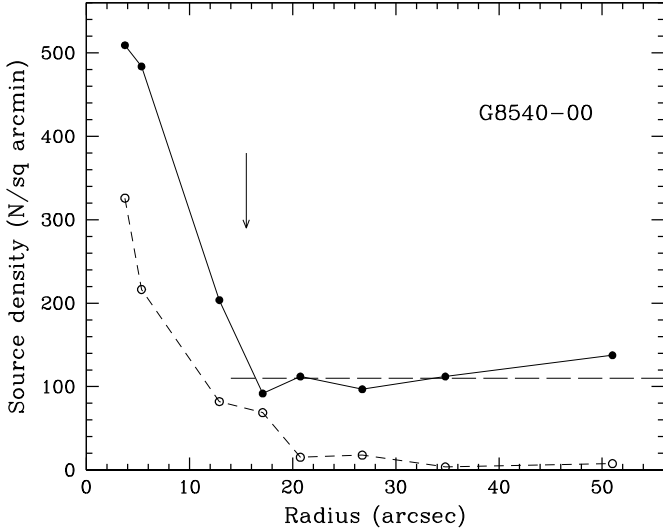


**Fig. 5.** Radial plots of the projected source density determined by counting sources in concentric rings on the  $K$ -band frame. The abscissa shows the mean radius of each measured ring centred at (J2000)  $\alpha = 20^{\text{h}}54^{\text{m}}14.2^{\text{s}}$ ,  $\delta = 44^{\circ}54'07.4''$ . Filled circles and the solid line refer to all sources detected in the  $K$  band, while open circles and the short-dashed line refer to sources with measured IR excesses, either from  $JHK$  and/or the IRAC colours. The long-dashed line is assumed to be the mean field source  $K$ -band density. Note that the IR-excess source density of the field is negligible.

( $r < 15.5''$ ), while open circles represent sources in our  $111'' \times 111''$  area but outside the circle. The infrared characteristics of each sample differ greatly from the other, particularly in the  $JHK$  regime: 34 of the 74 sources (46%) lying within the cluster area display significant excess emission at  $\lambda \geq 2 \mu\text{m}$  (that is, lying on the two-colour diagrams at least 0.2 mag to the right of the reddening line of OB-type photospheres). In contrast, only 25 of the 329 (8%) sources in the surrounding field show IR excess and, as clearly seen on the two-colour diagrams in Fig. 6, the magnitude of their IR-excess emission is considerably lower than that of their cluster area counterparts. Indeed, 68% of the sources with  $H - K$  colour-excess indices higher than 0.5 magnitudes lie within the cluster circle, although this occupies 0.07 times the field area.

Described from a different perspective, if the observed source density in the outside (field) area is assumed to be representative of the local line-of-sight field, then we would expect to find only 22 sources inside the cluster area, of which only 2 would display IR excesses. This implies that the likely number of members of the embedded cluster located in the present survey (i.e. the number of sources actually detected minus the number of expected ones) within a  $31''$  diameter is 52, and no fewer than 32 of them (62%) show considerable near-infrared excess emission, most probably originating in circumstellar discs. Indeed, this number is increased by at least 10 members with large infrared excesses seen at longer wavelengths (i.e. IRAC colours). It is important to bear in mind that at 8.0 kpc, our sensitivity only permits the detection of cluster members with  $M_K < 2.5$ , which corresponds to a F5 main-sequence star.

It is acknowledged that the best photometric diagnostics for the presence of discs are obtained by observations at  $\lambda > 3 \mu\text{m}$ , and to provide these, the *Spitzer* IRAC images are ideally suited. Unfortunately, for the compact cluster CBJC-8, the extremely bright emission of the two dominant mid-IR sources near the

cluster centre made it impossible to photometrically measure faint ones close to the nucleus. This was further aggravated by the *Spitzer* poor spatial resolution, especially when compared with our NICS images. For this reason, photometry for only 30 sources in the [3.6] and [4.5] bands could be obtained with precision of at least  $5\sigma$  over the noise. These sources are plotted in the  $H - K$  versus  $K - [3.6]$  diagram, shown in Fig. 6 (right panel). In this sample, 17 sources were found to have  $1.6 - 3.6 \mu\text{m}$  colours of normal photospheres, of which 5 are heavily reddened ( $A_V \approx 25 - 30$ ), plus another 3 sources have  $E(K - [3.6]) \approx 0.5$ , each suffering different amounts of extinction. Finally, 10 other sources display very large excesses at  $\lambda > 3 \mu\text{m}$ .

It is worth mentioning that only 12 sources were measurable (above  $5\sigma$ ) in all four IRAC bands, whose corresponding [3.6]–[4.5] vs. [4.5]–[5.8] and [3.6]–[4.5] vs. [5.8]–[8] diagrams are shown in Fig. 7. The colour indices of 3 of them are those of reddened field late-type stars, and the colours of the other bright 9 sources imply strong infrared excesses, indicative of the presence of discs that dominate the far-IR emission, confirming the near-IR analyses. These are the most luminous objects found in the present work and, except for one, their positions on the IRAC two-colour diagrams correspond to the region populated by very young Class I sources (Allen et al. 2004; Guieu et al. 2009). These objects are labeled with the letters A, B, C, D, E, F, G and J in Figs. 6 and 7. Source H is located close to the edge of the Class II box.

In summary, the very high fraction of IR-excesses (discs) found in the area covered by the cluster CBJC 8, including several with mid-IR colours of Class I objects, confirms a very young age, not higher than a few tenths of megayears. In Table 2 we present a list with coordinates and  $1 - 8 \mu\text{m}$  magnitudes of all IR-excess sources that are considered to be members of this young cluster (see also Sect. 3.3).

### 3.2. Spectral energy distributions of the young luminous sources

From the present photometry (Tables 1 and 2) we constructed the spectral energy distributions (SEDs) of the nine sources with large infrared excesses that were measured in the four IRAC bands. These are displayed in Fig. 8. We also derived infrared luminosities by integrating their SEDs, assuming a common distance of 8.0 kpc. In addition, we computed the infrared spectral indices  $\alpha(\text{IR})$  between 2.2 and  $8 \mu\text{m}$  for sources C, D, E, F, G, H, and J, and between 2.2 and  $12.7 \mu\text{m}$  for sources A and B. These values, summarized in Table 3, further confirm the extreme youth of these bright cluster members and provide a glimpse of the characteristics of upper luminosity function of this very young and distant cluster, which we will further discuss in Sect. 3.3.

We paid particular attention to the most luminous object, source A in the nucleus of CBJC 8. Its position coincides with that of a 6.7 GHz methanol maser and with the radio-continuum source detected at 6 cm by Urquhart et al. (2009) during their RMS survey (see Fig. 9). In addition, the SCUBA Legacy catalogue reports an extended (effective radius of  $61''$ ) sub-millimeter source at 450 and  $850 \mu\text{m}$  (Di Francesco et al. 2008) very close to this position. We constructed its SED (from 1.6 to  $850 \mu\text{m}$ ) with all the available photometric information (14 datapoints, see Fig. 10), including flux measurements at  $21.3 \mu\text{m}$  (*MSX*) and  $70 \mu\text{m}$  (*MIPS*). Given that the SED covers a wide range of frequencies and that, except in the submillimeter regime, the apertures included all the expected emission ( $r = 5000 - 30\,000 \text{ AU}$  at 8.0 kpc), we fitted the observed

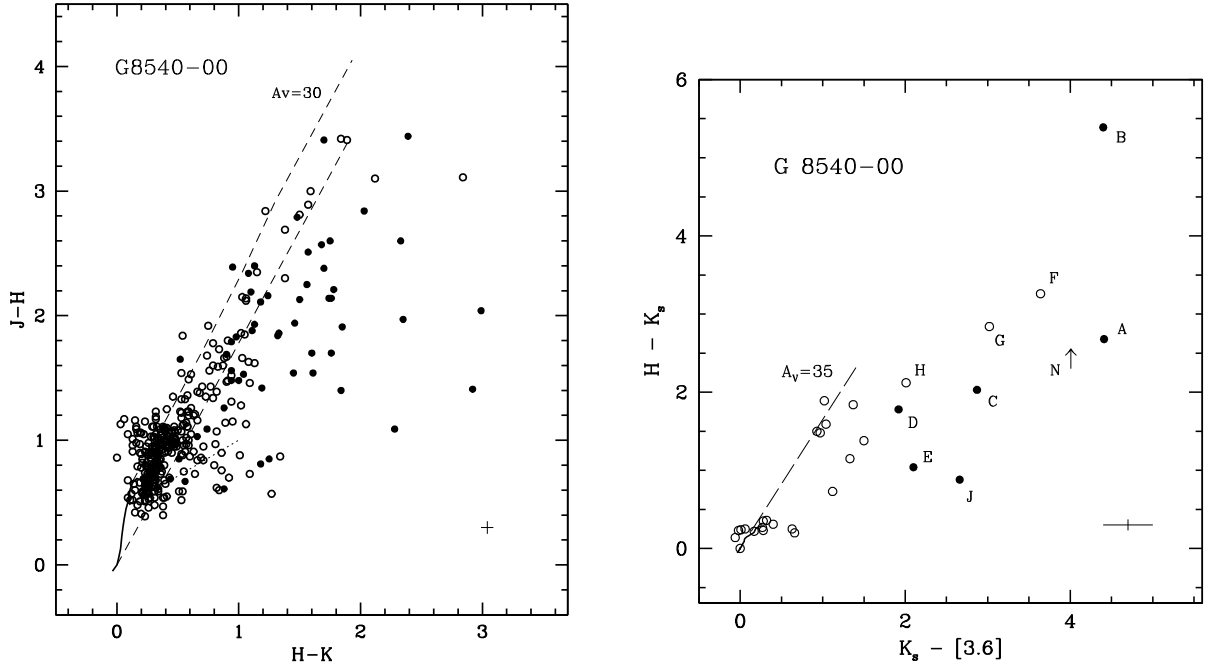


**Fig. 6.** *Left panel:*  $J - H$  versus  $H - K$  diagram. The filled circles represent sources located within a radius of  $15.5''$ , the formal limits of the embedded cluster. The open circles represent sources that lie outside this circle. The solid line marks the loci of the main-sequence (MS) stars from Koornneef (1983), while the dashed lines define the reddening band extending from the MS using the reddening vector from Rieke & Lebofsky (1985). *Right panel:*  $H - K$  vs.  $K - [3.6]$  diagram for the sources that could also be measured on the IRAC [3.6] images. Symbols are as in the left panel. In both, the reddening vector (broken line) is from Tapia (1981) and the loci of the MS (solid line), from Koornneef (1983); the crosses near the lower right corners show the mean statistical error of the individual measurements.

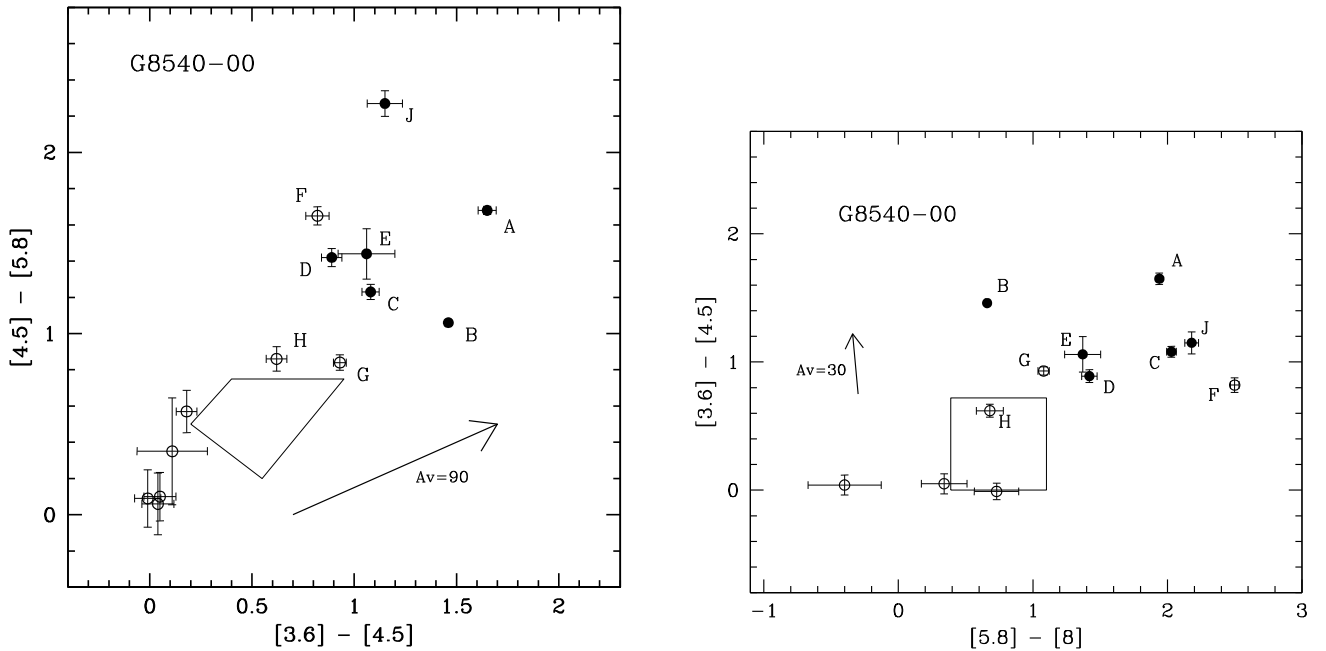


**Fig. 7.** IRAC colour-colour diagrams of the region centred on G8540-00. *Left panel:*  $[4.5] - [5.8]$  vs.  $[3.6] - [4.5]$  colours. *Right panel:*  $[3.6] - [4.5]$  vs.  $[5.8] - [8]$  colours. In both, the boxes mark the location of Class II young stellar objects and the arrows represent the extinction vector (Allen et al. 2004; Guieu et al. 2009). The position of the young sources believed to belong to the cluster are marked with the labels A, B, C, D, E, F, G, H, J, and N. Note that object H is at the edge of the box of class II sources; the others lie in the area occupied by Class I objects.

SED with the infalling envelope+disc+central source radiation transfer model described by Robitaille et al. (2006) by using the fitting tool of Robitaille et al. (2007). These authors computed a grid of 20 000 models covering a large variety of possible physical parameters of the central stars, discs and envelopes under 10 viewing (inclination) angles and their fitting routine selects

those models that fit the data best on the basis of the values of  $\chi^2$ . Normally, those fits complying the criterium  $\chi^2_{\text{best}}/\text{datapoint} - \chi^2_{\text{best}}/\text{datapoint} < 2-3$  are considered well fitted (for a discussion on the possible caveats of the models and routines, see Robitaille et al. 2007). For source A, we introduced several constraints, namely the assumed distance (7.9–8.1 kpc) and an acceptable

**Table 2.** Coordinates and *JHK* and IRAC magnitudes of the sources with *K*-band excesses in the central region within 30'' of G85.40-0.00.

ID	$\alpha(2000)$			$\delta(2000)$			<i>J</i> mag	<i>H</i> mag	<i>K</i> mag	[3.6] mag	[4.5] mag	[5.8] mag	[8] mag
	h	m	s	°	'	''							
1 (H)	20	54	12.16	44	54	15.8	18.14 (0.02)	15.04 (0.01)	12.92 (0.01)	10.91 (0.04)	10.29 (0.03)	9.43 (0.06)	8.75 (0.08)
2 (D)	20	54	12.78	44	54	08.1	16.78 (0.01)	14.57 (0.01)	12.79 (0.01)	10.87 (0.04)	9.98 (0.03)	8.56 (0.04)	7.14 (0.04)
3	20	54	12.96	44	54	07.1	–	>18.0	15.81 (0.04)	–	–	–	–
4	20	54	13.13	44	54	07.3	21.48 (0.17)	20.07 (0.15)	17.15 (0.05)	–	–	–	–
5	20	54	13.40	44	54	00.0	19.82 (0.07)	18.73 (0.04)	16.45 (0.02)	–	–	–	–
6	20	54	13.47	44	54	08.6	18.33 (0.01)	17.52 (0.02)	16.34 (0.01)	–	–	–	–
7	20	54	13.49	44	54	7.1	19.73 (0.04)	17.16 (0.03)	15.48 (0.04)	–	–	–	–
8	20	54	13.50	44	54	17.4	–	19.62 (0.20)	16.78 (0.05)	–	–	–	–
9	20	54	13.51	44	54	13.7	21.00 (0.15)	19.60 (0.16)	17.76 (0.09)	–	–	–	–
10 (A)	20	54	13.60	44	54	07.7	–	16.35 (0.03)	13.67 (0.01)	9.26 (0.04)	7.61 (0.02)	5.93 (0.01)	3.99 (0.01)
11 (N)	20	54	13.60	44	54	01.9	–	>18.2	15.81 (0.08)	10.89 (0.25)	9.59 (0.25)	–	–
12	20	54	13.70	44	54	06.5	19.47 (0.04)	17.56 (0.04)	15.71 (0.07)	–	–	–	–
13	20	54	13.75	44	54	05.7	19.56 (0.05)	17.43 (0.03)	15.93 (0.05)	–	–	–	–
14	20	54	13.82	44	54	8.6	–	18.53 (0.09)	15.66 (0.04)	–	–	–	–
15	20	54	13.83	44	54	14.8	18.65 (0.04)	16.51 (0.02)	14.75 (0.01)	–	–	–	–
16	20	54	13.85	44	54	07.0	20.21 (0.06)	17.61 (0.03)	15.28 (0.03)	–	–	–	–
17	20	54	13.91	44	54	06.3	20.19 (0.06)	17.94 (0.04)	16.38 (0.04)	–	–	–	–
18 (E)	20	54	13.91	44	54	21.6	17.17 (0.01)	15.64 (0.01)	14.60 (0.01)	12.50 (0.12)	11.44 (0.07)	10.00 (0.12)	8.63 (0.06)
19 (C)	20	54	13.94	44	54	13.5	17.92 (0.02)	15.08 (0.02)	13.05 (0.03)	10.18 (0.03)	9.10 (0.03)	7.87 (0.03)	5.84 (0.02)
20	20	54	13.95	44	54	05.4	21.18 (0.13)	18.58 (0.05)	16.83 (0.04)	–	–	–	–
21	20	54	14.06	44	54	12.4	19.33 (0.03)	17.39 (0.05)	15.93 (0.04)	–	–	–	–
22	20	54	14.07	44	53	59.9	19.20 (0.06)	17.50 (0.03)	15.90 (0.01)	–	–	–	–
23	20	54	14.07	44	54	08.3	–	17.76 (0.07)	15.39 (0.04)	–	–	–	–
24	20	54	14.14	44	54	08.8	21.63 (0.20)	19.59 (0.09)	16.60 (0.03)	–	–	–	–
25	20	54	14.19	44	54	13.9	17.57 (0.02)	16.96 (0.05)	16.08 (0.08)	–	–	–	–
26	20	54	14.31	44	54	12.8	18.51 (0.04)	17.09 (0.04)	15.90 (0.05)	–	–	–	–
27 (B)	20	54	14.34	44	54	04.6	–	16.68 (0.03)	11.29 (0.01)	6.89 (0.01)	5.43 (0.01)	4.37 (0.01)	3.71 (0.01)
28	20	54	14.36	44	53	57.3	20.93 (0.12)	18.55 (0.04)	16.85 (0.04)	–	–	–	–
29	20	54	14.37	44	54	10.9	20.42 (0.09)	18.56 (0.08)	17.23 (0.06)	–	–	–	–
30 (F)	20	54	14.40	44	53	34.2	–	17.86 (0.04)	14.56 (0.01)	11.13 (0.04)	10.31 (0.04)	8.66 (0.03)	6.18 (0.01)
31 (Bc)	20	54	14.46	44	54	04.8	19.89 (0.06)	16.45 (0.02)	14.06 (0.03)	–	–	–	–
32 (J)	20	54	14.50	44	53	56.7	16.58 (0.01)	15.32 (0.01)	14.44 (0.01)	11.78 (0.07)	10.63 (0.05)	8.36 (0.05)	7.41 (0.08)
33 (G)	20	54	14.56	44	53	39.5	17.98 (0.02)	14.87 (0.01)	12.03 (0.01)	9.01 (0.01)	8.08 (0.01)	7.24 (0.01)	6.16 (0.01)
34	20	54	14.60	44	53	59.4	–	20.55 (0.16)	17.94 (0.09)	–	–	–	–
35	20	54	14.61	44	53	52.8	21.96 (0.22)	19.82 (0.10)	18.08 (0.11)	–	–	–	–
36	20	54	14.81	44	54	03.2	21.59 (0.24)	19.62 (0.17)	17.27 (0.07)	–	–	–	–
37	20	54	14.83	44	54	16.2	–	20.29 (0.19)	17.46 (0.06)	–	–	–	–
38	20	54	14.85	44	54	11.3	20.27 (0.07)	18.73 (0.06)	17.28 (0.07)	–	–	–	–
39	20	54	14.88	44	54	15.2	18.91 (0.04)	18.06 (0.06)	16.81 (0.07)	–	–	–	–
40	20	54	14.89	44	54	14.0	21.29 (0.13)	19.59 (0.13)	17.83 (0.09)	–	–	–	–
41	20	54	15.04	44	53	54.8	20.85 (0.11)	19.01 (0.04)	17.69 (0.08)	–	–	–	–
42	20	54	15.17	44	54	02.2	20.85 (0.12)	19.31 (0.10)	17.70 (0.08)	–	–	–	–
43	20	54	15.49	44	54	42.1	18.80 (0.03)	16.50 (0.01)	15.12 (0.02)	13.62 (0.15)	13.75 (0.27)	–	–
44	20	54	15.95	44	54	30.7	16.95 (0.01)	15.60 (0.01)	14.87 (0.01)	13.75 (0.18)	12.95 (0.14)	–	–

range of values of  $A_V$  that must be compatible with the position of the source on the infrared colour-colour and colour-magnitude diagrams. These suggest that  $A_V$  cannot be larger than 55 or much smaller than 48. Another known parameter whose fitted value must be satisfied a priori is the effective temperature of the central star which, as discussed in the next paragraph, has to be  $\log T_{\text{eff}} \sim 4.5$ . The physical parameters for the best-fit model are listed in Table 4. The only other model that satisfied the goodness of fit criterium  $\chi^2/\text{datapoint} - \chi_{\text{best}}^2/\text{datapoint} < 1$  yielded not too discordant values of most of the disk and envelope parameters (i.e. less than a factor of 2), and the same inclination angle, but required a totally implausible value of  $A_V$  towards the central star. None of the other fitted models could be considered acceptable as they implied  $\chi^2$  criteria, which were 50 times worse. The adopted model fits well the observations up to 70  $\mu\text{m}$  (see Fig. 10), though the discrepancies are considerable with the sub-millimeter points. This is understood in terms of the extended nature of the SCUBA-mapped submillimeter emission,

which represents the natal clump from which the whole cluster has formed instead of being associated with the single object (source A). We did not attempt to repeat this exercise for the other sources in Table 3, as the number of data points that define their SEDs ( $\lambda < 9 \mu\text{m}$ ) is considerably smaller and the uncertainties of the model would be far greater than for source A.

As is known to be the pattern for high-mass clusters, the most luminous and, presumably, most massive young objects are located at the nucleus of CBJC 8. Sources A and B dominate the mid-IR luminosity of the whole system, though the former is the brightest source at  $\lambda > 9 \mu\text{m}$ . At  $d = 8$  kpc, the total luminosity of source A is found to be about  $5.0 \times 10^4 L_{\odot}$  (Table 3), which corresponds to a 09.5 – B1 V star (Crowther 2005). As mentioned earlier, this object is associated with a compact HII region (see Fig. 9), for which Urquhart et al. (2009) measured a 6 cm radio continuum flux of 31.2 mJy. For an optically thin HII region and assuming  $N_e = 10^4$  K, we used Schraml & Mezger's (1969) relations to derive the number of UV ionizing photons

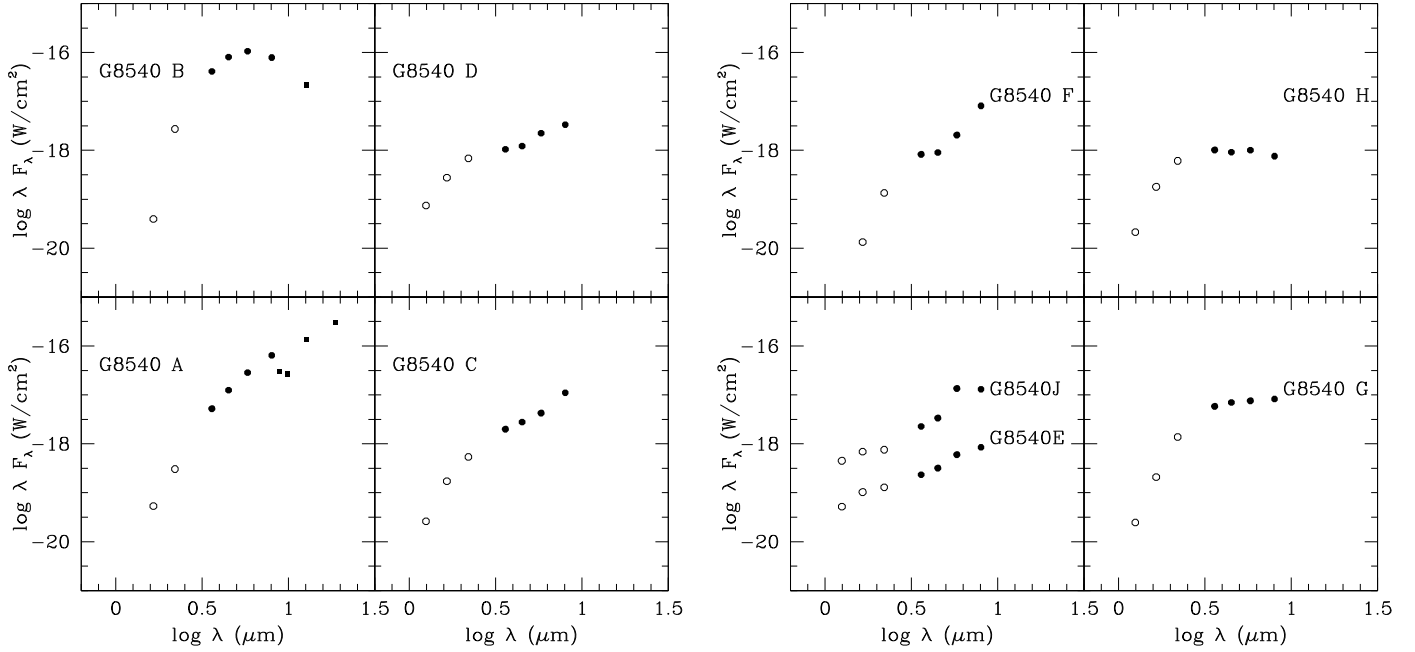


**Fig. 8.** Spectral energy distributions of sources A, B, C, D, E, F, G, H and J in G8540-0.00. Open and filled circles represent the NICS near-infrared and IRAC data, while the filled squares are the CID mid-IR flux densities. For clarity, the SED of source J has been scaled up by a factor of five.

**Table 3.** Infrared (1.2–8  $\mu\text{m}$ ) luminosities and spectral indices for the sources G8540 A, B, C, D, E, F, G, H, and J.

Source	$L(\text{IR})$ $L_{\odot}$	$\alpha(\text{IR})$
G8540 A	49 000 <sup>*</sup>	3.49
G8540 B	6600 <sup>+</sup>	2.60
G8540 C	415	2.34
G8540 D	178	1.23
G8540 E	46	3.24
G8540 F	240	3.17
G8540 G	604	1.38
G8540 H	90	0.17
G8540 J	136	2.21

**Notes.** (<sup>\*</sup>) Total luminosity from Table 4 for  $d = 8$  kpc. (<sup>+</sup>) Infrared luminosity from 1.2 to 12.7  $\mu\text{m}$ .

**Table 4.** Physical parameters of G8540-00A from the best-fit Robitaille et al. (2006) model.

Stellar mass ( $M_{\odot}$ )	18
Stellar temperature (K)	$3.3 \times 10^4$
Envelope and disc inner radii ( $R_{\text{sub}}$ )	1.5
Envelope cavity angle (degrees)	14
Envelope accretion rate ( $M_{\odot} \text{ yr}^{-1}$ )	$3.0 \times 10^{-3}$
Envelope mass ( $M_{\odot}$ )	$1.7 \times 10^3$
Disc outer radius (AU)	40
Disc mass ( $M_{\odot}$ )	0.3
Disc accretion rate ( $M_{\odot} \text{ yr}^{-1}$ )	$2.1 \times 10^{-4}$
Inclination angle (degrees)	18
$L_{\text{bol}}/L_{\odot}$	$4.8 \times 10^4$
$A_V$	48
Distance (kpc)	8.1

required to maintain this flux (see also Carpenter et al. 1990). This number is  $2 \times 10^{47} \text{ s}^{-1}$ , which is provided by a B0–B0.5 V star (Panagia 1973), similar to that implied by its bolometric

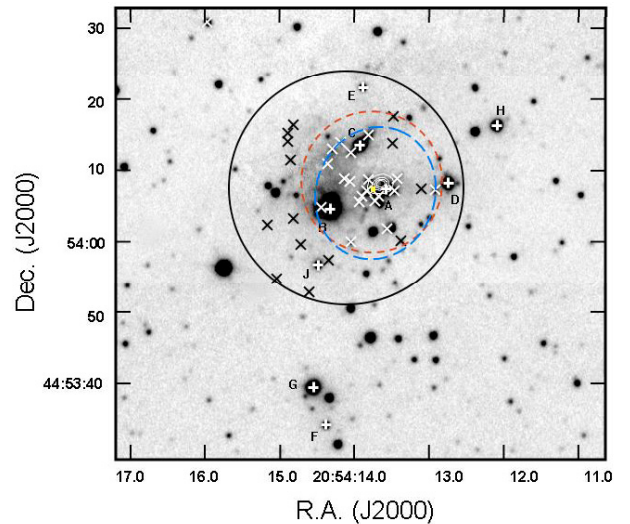


**Fig. 9.** K-band image of the central region of G85.40-0.00 showing the spatial distribution of the IR-excess sources, believed to be cluster members, listed in Table 2. The signs  $\times$  refer to those sources with  $K$ -band excesses or have  $H - K > 2$  and are too faint to be detected in  $J$ , and the signs  $+$  refer to those sources with four measured IRAC colours. The 6 cm contours (Urquhart et al. 2009) are superimposed in white. The position of the methanol maser is marked with a yellow square, while the highest contours on the SCUBA 850  $\mu\text{m}$  and MIPS 70  $\mu\text{m}$  maps are shown schematically with long (red) and short (blue) dashed lines, respectively. A colour version of this figure is available in the electronic edition.

luminosity. The nearby source B, for which we can only determine its infrared (1 to 13  $\mu$ ) luminosity of  $6.6 \times 10^3 L_{\odot}$  (Table 3), has a total luminosity of probably a factor of 1.5 to 2 higher (see SED in Fig. 10), which would correspond to a B2–B3 V star (Crowther 2005); such a star would emit no more than  $10^{45}$  UV photons (Panagia 1973), sufficient to ionize the surrounding gas and produce a small HII region. Its free-free emission would be observable at 6 cm, with a flux density of approximately 0.1 mJy,

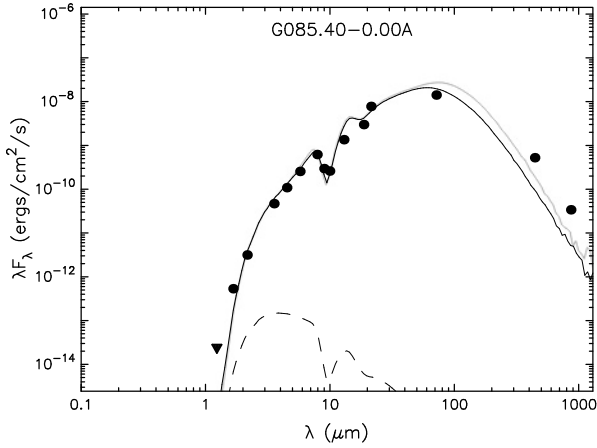


**Fig. 10.** Spectral energy distribution (SED) of source G8540A using the NICS (1.2 to 2.2  $\mu\text{mm}$ ), IRAC (3.6 to 8  $\mu\text{mm}$ ), CID (9 to 17  $\mu\text{mm}$ ), MSX (23  $\mu\text{mm}$ ), MIPS (70  $\mu\text{mm}$ ) and SCUBA (450 and 850  $\mu\text{mm}$ ) measurements. The two best-fit models of the SED derived from the Robitaille et al. (2007) fitting tool are over-plotted with solid lines. The dashed line represents the stellar photosphere used as input to the radiation transfer code. The parameters of the model that best fit the SED (dark solid line) are listed in Table 4.

well below the sensitivity of Urquhart et al.’s (2009) radio survey. Indeed, this source was not detected.

### 3.3. Magnitude-colour diagram and cluster characteristics

Colour-magnitude diagrams provide the best photometric diagnostics of stellar clusters of all ages. For deeply embedded clusters, as in our study, the  $K$  versus  $H - K$  diagram is the one that gives better information on the physical properties of the cluster as a whole as well as of the individual members. In Fig. 11 we present this diagram for all sources measured on our NICS  $H$  and  $K$  images. The sample was divided into four subsets: (i) the 32 sources located within the cluster area that showed no indication of IR excess; (ii) the 35 sources, also within the cluster area, with significant IR-excesses; (iii) the 304 sources found lying outside the cluster area with colours of reddened photospheres, and (iv) those outside (25) with IR-excess. Each of these groups is plotted in the colour-magnitude diagram with a different symbol

Let us first consider the sources inside the  $r = 15.5''$  circle, most of which are expected to be physical members of the embedded cluster (see Sect. 3.1). We found that 82% of them have  $H - K > 0.9$ ; indeed, several objects that do not show any IR excess are aligned almost horizontally on the colour-magnitude diagram, with  $H - K$  around 1.0, with a range of more than 4 magnitudes in  $K$ . Considering the very young age of the cluster, it is reasonable to compare their location with regard to the  $10^5$  yr isochrone (from Palla & Stahler’s 1999 model) that fit these points in the colour-magnitude diagram for a distance of 8.0 kpc. The results are shown in Fig. 11. The implied value of the extinction is  $A_V = 12.5$ . As expected statistically, we found 14 foreground sources in the cluster area that fall to the left of this sequence. Also, a few non-excess stars are located to the right of this sequence implying extra amounts (up to of  $A_V = 5$ ) of extinction.

The striking feature of this plot, however, is the large number (29) of sources in the cluster area with large IR-excess that are scattered all over the diagram with  $H - K > 1.2$ , with  $K$  magnitudes ranging from 11 to 18. The brightest objects in the  $K$  band with infrared luminosities higher than  $50 L_\odot$  (Sect. 3.2)

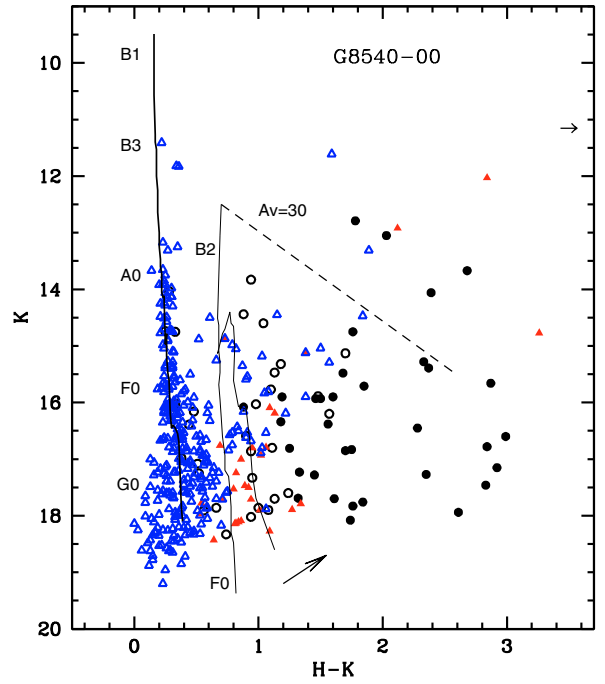


**Fig. 11.**  $K$  versus  $H - K$  diagram of all sources with  $HK$  colours. Filled, black circles represent sources within  $r < 15.5''$  with considerable IR-excesses (at  $\lambda > 2 \mu\text{m}$ ). The small horizontal arrow points to the position of source B, with  $H - K = 5.39$ . Open black circles have  $JHK$  colours of reddened photospheres. Sources outside the cluster area are plotted as triangles; filled symbols (red) show infrared excesses and open (blue) symbols do not. For reference, the thick solid line marks the loci of the main-sequence (MS) stars from Koornneef (1983) for a distance of 2.5 kpc and reddened by  $E(H - K) = 0.2$ , corresponding to  $A_V = 4.2$ . The thin continuous line represents the ZAMS and  $10^5$  yr isochrone (Palla & Stahler 1999) for a distance of 8.0 kpc and reddening of  $E(H - K) = 0.75$  ( $A_V = 12.5$ ), parameters that seem to fit the likely cluster members with no infrared excess. The short-dashed line defines the reddening vector from Rieke & Lebofsky (1985) and the long arrow marks the average slope of near-infrared excesses caused by discs around young stellar objects, as determined by Salas et al. (2006). A colour version of this figure is available in the electronic edition.

are listed in Table 3. Note that three of these nine luminous objects (F, G and H), as well as two fainter ones, are located outside the formal limits of the cluster (see Fig. 9), at radii from  $20''$  to  $35''$ ; but their IR diagnostics definitely indicate that they are bona-fide cluster members that at present appear out-of-bounds as a consequence of using star densities that are naturally weighted towards faint, low-mass stars to define the circle delimiting the cluster.

Although it is impossible to assign a single age to the cluster CBJC 8 from the present data, the very large scatter of IR-excess sources to the right-hand side of the  $K$  versus  $H - K$  diagram indicates a large disc population with a considerable variety of circumstellar disc properties. Indeed, this large fraction of discs suggests that the cluster formation started less than  $3 \times 10^6$  years. By simply adding the estimated masses of the observed cluster members listed in Table 2, we can put a lower limit to the cluster stellar mass of around  $140 M_\odot$ .

Finally, as also described in Sect. 3.1, the great majority (87%) of the 304 sources outside the cluster area are reddened photospheres, which are representative of the field towards this line-of-sight. Most of these have  $H - K < 0.7$  and a few, as

expected statistically, show moderate infrared excess. This sample, distributed uniformly over the whole of our observed field, consists mainly of foreground stellar objects, and it is surprising that for  $K < 16.5$ , the great majority seem to define, in the colour-magnitude and colour-colour diagrams (Figs. 6 and 11), a main sequence that is best fitted by a distance of 2.5 kpc and  $A_V = 12.5$ , as illustrated in Fig. 11. Studying the properties of this population, like testing whether it belongs to the NAPN (known to be at  $d = 600$  pc, Guieu et al. 2009) or otherwise, is beyond the scope of this work.

### 3.4. Hydrogen molecular emission

In the imaged area we found only one faint and unresolved knot emitting in the  $H_2 v = 1, 0 S(1)$  line at the position  $\alpha = 20^h54^m14.45^s$ ,  $\delta = 44^\circ54'00.0''$  (J2000). This small molecular hydrogen emission nebula, presumably shock-excited, represents the only observational indication of the likely presence of mass outflows in the region of G85.40-0.00, as would be expected to be associated with such a young cluster. The observed emission knot lies only  $4.6''$  south of the very red source B and  $3.4''$  north of the less luminous one, J (see, Figs. 2 and 9). Based on the available observations, it is impossible to determine which object is responsible for powering this outflow and exciting the observed  $H_2$  knot. To understand this, we need to wait until high-resolution CO mapping is made towards this region.

## 4. Conclusions

We have obtained new high-sensitivity and sub-arcsec resolution near- and mid-infrared images centred on the young stellar cluster CBCJ 8 discovered by Cambr esy et al. (2002). From the analysis of these and archive *Spitzer* IRAC images we derive the following conclusions:

- 1) Forty-four near-infrared sources with significant excess emission at  $\lambda \geq 2 \mu\text{m}$  were found, mostly within a circular area of radius  $15.5''$ . This confirms the presence of an embedded stellar cluster composed by very young stars with circumstellar disks. For an assumed distance of 8 kpc from the Sun, the individual luminosities range from two to a few tens of thousand solar luminosities. The total stellar mass is estimated to be in excess of  $140 M_\odot$ .
- 2) The eight most luminous sources, labelled G8540 A, B, C, D, E, F, G and J, were measured in the four IRAC-bands and found to exhibit large infrared excess emission, characterized by large ( $\alpha > 1$ ) infrared spectral indices, indicating very young ages. The mid- to far-infrared emission is dominated by sources A and B. The former has a luminosity

of approximately  $5 \times 10^4 L_\odot$ . A 6.7 GHz methanol maser G85.40-0.00 (Pestalozzi et al. 2005) and an ultracompact 6 cm radio source G085.4102+00.0032 (Urquhart et al. 2009) are associated with this source. The observed 1.6 to  $850 \mu\text{m}$  fluxes of this system were well fitted by using Robitaille et al.'s (2007) model of an infalling envelope plus disc plus central star to obtain an idea of its likely physical properties.

- 3) A molecular hydrogen emission knot was detected around the centre of the cluster, providing evidence of at least one outflow in this young complex. Several young sources detected in the vicinity of the small nebula may be responsible for driving this outflow.

*Acknowledgements.* We acknowledge Dr. James Urquhart, whose suggestions led to a substantial improvement of this paper. We appreciate Dr. B. Whitney's suggestions to improve the SED fitting of G8540-00A. M.T. acknowledges PAPIIT No. IN-100210 from DGAPA/UNAM.

## References

- Allen, L.E., Calvet, N., D'Alessio, P., et al. 2004, *ApJS*, 154, 363  
 Bica, E., Dutra, C. M., & Barbuy, B. 2003a, *A&A*, 397, 177  
 Bica, E., Dutra, C. M., Soares, J., & Barbuy, B. 2003b, *A&A*, 404, 223  
 Bohigas, J., & Tapia, M. 2003, *AJ*, 126, 1861  
 Bonnell, I. A., & Bates, M. R. 2006, *MNRAS*, 370, 488  
 Brand, J., & Blitz, L. 1993, *A&A*, 275, 67  
 Cambr esy, L., Beichman, C. A., Jarrett, T. H., et al. 2002, *AJ*, 123, 2559  
 Carpenter, J. M., Snell, R. L., & Schloerb, F. P. 1990, *ApJ*, 362, 147  
 Crowther, P. A. 2005, *IAU Symp.*, 227, 389  
 Di Francesco, J., Johnstone, D., Kirk, H., et al. 2008, *ApJS*, 175, 277  
 Dutra, C. M., Bica, E., Soares, J., & Barbuy, B. 2003, *A&A*, 400, 533  
 Guieu, S., Rebull, L. M., Stauffer, L. A., et al. 2009, *ApJ*, 697, 787  
 Hunt, L. K., Mannucci, F., Testi, L., et al. 1998, *AJ*, 115, 2594  
 Koornneef, J. 1983, *A&A*, 128, 84  
 Lada, C. J., & Lada, E.A. 2003, *ARA&A*, 41, 57  
 Palla, F. A., & Stahler, F. W. 1999, *ApJ*, 525, 771  
 Panagia, N. 1973, *AJ*, 78, 929  
 Persson, S. E., Murphy, D. C., Krzeminski, W., et al. 1998, *AJ*, 116, 2475  
 Pestalozzi, M. R., Minier, V., & Boot, R. S. 2005, *A&A*, 432, 737  
 Rieke, G. H., & Lebofsky, M. J. 1985, *ApJ*, 288, 618  
 Robitaille, T. P., Whitney, B. A., Indebetouw, R., Wood, K., & Denzmore, P. 2006, *ApJS*, 167, 256  
 Robitaille, T. P., Whitney, B. A., Indebetouw, R., & Wood, K. 2007, *ApJS*, 169, 328  
 Salas, S., Cruz-Gonzalez, I., & Tapia, M. 2006, *Rev. Mex. Astron. Astrofis.*, 42, 273  
 Schraml, J., & Mezger, P.G. 1969, *ApJ*, 156, 269  
 Skrutskie, M. F., Cutri, R. M., Stiening, R., et al. 2006, *AJ*, 131, 1163  
 Stetson, P. B. 1987, *PASP*, 99, 191  
 Tapia, M. 1981, *MNRAS*, 197, 949  
 Urquhart, J. S., Busfield, A. L., Hoare, M. G., et al. 2008a, *A&A*, 487, 253  
 Urquhart, J. S., Hoare, M. G., Lumsden, S. L., Oudmaijer, R. D., & Moore, T. J. 2008b, *ASPCs*, 387, 381  
 Urquhart, J. S., Hoare, M. G., Purcell, C. R., et al. 2009, *A&A*, 501, 539